Effect of natural and calcined halloysite clay minerals as low-cost additives on the performance of 3D-printed alkali-activated materials

Mehdi Chougan [a], Seyed Hamidreza Ghaffar [a,b,*], Behzad Nematollahi [c], Pawel Sikora [d], Tobias Dorn [e], Dietmar Stephan [e], Abdulrahman Albar [a], Mazen J Al-Kheetan [f,g]

[a] Department of Civil and Environmental Engineering, Brunel University London, Uxbridge UB8 3PH, United Kingdom
[b] Applied Science Research Center, Applied Science Private University, Jordan
[c] Department of Civil and Structural Engineering, The University of Sheffield, Sheffield S1 3JD, United Kingdom
[d] Faculty of Civil and Environmental Engineering, West Pomeranian University of Technology in Szczecin, Al. Piastow 50, 70-311 Szczecin, Poland
[e] Department of Building Materials and Construction Chemistry, Technische Universität Berlin, Gustav-Meyer-Allee 25, 13355 Berlin, Germany
[f] Civil and Environmental Engineering Department, College of Engineering, Mutah University, P.O. Box 7, Mutah, Karak, Jordan
[g] Materials Science and Energy Lab, MSEL, Mutah University, P.O. Box 7, Mutah, Karak, Jordan

HIGHLIGHTS

- Natural and calcined Halloysite clay additives were characterised.
- Halloysite clay additives were incorporated to modify AAMs' printing properties.
- Enhanced compatibility of calcined Halloysite clay additives in the AAMs was verified.
- Buildability and mechanical properties were improved in CH-modified AAMs.

GRAPHICAL ABSTRACT
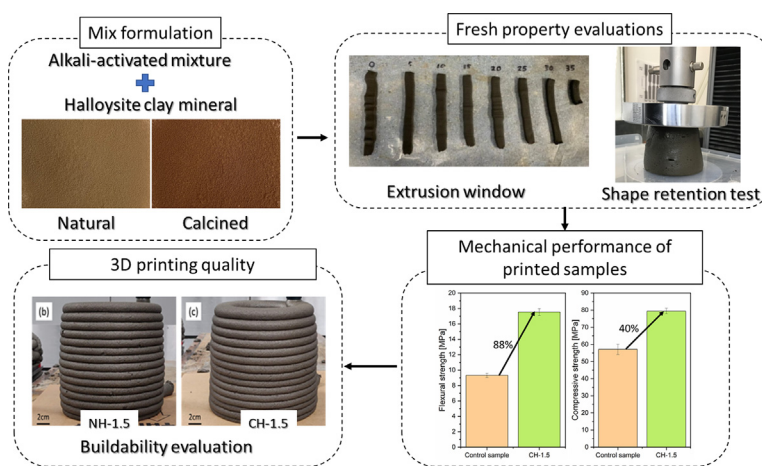
ARTICLE INFO

ABSTRACT

This study investigates the effects of natural and calcined halloysite clay minerals ("NH" and "CH", respectively) on the performance of 3D printed alkali-activated materials (AAMs). Halloysite clay minerals are selected as they are low-cost and abundantly available. At first, different characterisation techniques were employed to characterise the NH and CH additives. Mechanical performance, extrusion window, and shape stability of several AAM formulations containing various dosages (0.5 wt% to 5 wt%) of the NH and CH additives were evaluated. The best-performing mixtures in terms of fresh and hardened properties namely, NH-1.5 and CH-1.5 mixtures (containing 1.5 wt% of NH and CH additives, respectively) were then selected for 3D printing. The results showed that the CH-1.5 mixture exhibited enhanced shape stability, buildability, and mechanical properties as compared to the control mixture. The flexural and compressive strengths of 3D printed CH-1.5 samples were 88% and 40%, respectively higher than those of the printed control samples. Using the CH-1.5 mixture, a twisted column with an intricate shape was printed to verify the suitability of the developed CH-modified AAM for the

* Corresponding author.
  E-mail address: seyed.ghaffar@brunel.ac.uk (S. Hamidreza Ghaffar).

construction of complex structures. This study establishes the use of halloysite clay minerals as low-cost additives for enhancing the mechanical properties and printing performance of AAMs.

1. Introduction

Concrete is the most used material on the earth [1]. The production of Ordinary Portland Cement (OPC), the main ingredient to make concrete, is a high-energy-consuming process with substantial CO_2 emissions, accounting for around 7% of annual CO_2 emissions [2]. With climate change and global warming emerging in recent years, a crucial need for some immediate actions to mitigate greenhouse gas emissions through cement manufacturing plants became essential [3]. Since the 1970 s, alkali-activated materials (AAMs) synthesised by a reaction between alkali activator and aluminosilicate source materials employing industrial products and by-products (e.g., fly ash, metakaolin, silica fume, and slag) have piqued public interest as a promising eco-friendly alternative to OPC [4,5].

The recent developments in the production of AAMs with high mechanical and durability characteristics have fulfilled the increasing demands in the building industry. The AAMs' characteristics, adjustable setting time and rheological properties make them an ideal feedstock for new emerging construction techniques such as 3D printing [6]. However, the application of AAMs in 3D printing is still very limited as compared to OPC. To enhance the performance of 3D printed AAM, several rheology modifiers and reinforcing additives, including polypropylene (PP) fibres [7,8], polyvinyl alcohol (PVA) fibres [9], attapulgite nano-clay particles [10], and graphene-based materials (GBM) [11], have been studied. However, such additives are costly. Thus, the search for low-cost additives that can enhance the performance of 3D printed AAMs becomes critical.

The introduction of nano additives could enhance the thixotropic behaviour of AAM mixtures by improving the contact forces, colloidal interactions, and hydrodynamic force between AAM's principal components [12–14]. The promising impact of nano-clay additives on the printing quality of AAMs has to be associated with their high aspect ratio, which makes nano-clays highly effective. Panda et al. reported that incorporating 0.5 wt% attapulgite nano-clay in the AAM increased thixotropic behaviour and 3D printing performance. However, 17% reduction in compressive strength was observed compared to the control sample [15]. Similar trends have been also reported in some of the authors' previous works, in which the incorporation of 1 wt% attapulgite nano-clay significantly improved the fresh properties of AAM composites [9]. It should be noted that attapulgite nano-clay has been mainly used as a rheology modifying agent.

This study, for the first time, investigates the use of halloysite clay minerals, as both reinforcing and rheology modifying additives, on the performance of 3D printed AAMs. Halloysite clay minerals are selected as they are low cost and abundantly available compared to other additives [16,17]. This category of aluminosilicate materials belongs to the kaolin group of minerals with the chemical formulation of $Al_2Si_2O_5(OH)_4 \cdot 2H_2O$. The structure of halloysite clay minerals is composed of 1:1 stacked layers built from tetrahedral (Si) and octahedral (Al) sheets. The layers are linked through hydrogen bonding formed between the oxygen atoms of the tetrahedral sheet and the inner surface OH groups of the octahedral sheet [18,19]. The presence, or former presence, of interlayer water, distinguishes halloysite from other minerals in the kaolin group [20]. There are several variations in the morphology of halloysite clay minerals, which most commonly include either halloysite tubules or plates. This structure facilitates the ability to activate both the surface tetrahedral and octahedral sheets.

This study investigates natural and calcined halloysite clay minerals with dosages between 0.5 wt-% and 5 wt-% in the AAMs. The mixtures were characterised by shape retention, mechanical and microstructural tests, and open time for extrusion. The best performing mixtures were then printed, and the mechanical and buildability properties were assessed and compared to the control AAM composite (with no halloysites clay mineral). The aim is to select the best performing dosage of halloysite clay minerals and examine their mechanical and rheology strengthening functionality. To the best of the authors' knowledge, no study on the implementation of halloysite clay additives in 3D printable AAMs has previously been carried out.

2. Materials

Fly ash (FA), complying with BS EN 450–1:2012 and supplied by Cemex, UK and ground granulated blast furnace slag (GGBS) provided by Hanson Heidelberg Cement, UK, complying with EN15167-1, were employed as the aluminosilicate source materials. The chemical composition of the FA and GGBS are presented in Table 1. Two grades of river sand (0 – 0.5 mm, and 0.5 – 1.0 mm) and quartz sand (0.06 – 0.3 mm) obtained from J. Stoddard & Sons Ltd were used as the aggregates. The alkaline activator was made by mixing 10 mol/l sodium hydroxide solution and sodium silicate solution with an alkali modulus of 3.23 (8.60 wt-% Na_2O, 27.8 wt-% SiO_2, 63.2 wt-% H_2O, and 0.4 wt-% Al_2O_3) with a 1:2 ratio (by mass). The authors' previous studies provide more information on materials characterisations, including raw materials' size distributions [9,11]. The natural halloysite clay material was obtained from Dunino deposit of weathered basalt (near Legnica, Lower Silesia, Poland), which is the largest halloysite clay minerals deposit in the world. The halloysite consists of nanotubes and nanoplatelets [21–24]. Calcined halloysite clay mineral (referred to as CH) was prepared by heating the natural halloysite clay minerals (referred to as NH) at 600 °C for 1 h in the electric muffle furnace FCF 2,5SM (Czylok, Poland). The chemical composition of the NH and CH additives are also presented in Table 1.

2.1. Characterisations of natural and calcined halloysite clay minerals

Fig. 1 depicts the SEM images of natural and calcined halloysite platelets, displaying the material's distinctive flaky texture. The shape of the flakes was irregular and heterogeneous. As shown in Fig. 1, it is evidenced that the halloysite platelets are destructed and broken during calcination process, resulting in the production of particles with smaller dimensions [25]. BET specific surface area of the CH sample was measured to be 57.05 m^2/g, while the corresponding value for the NH sample was measured to be 67.87 m^2/g. The specific gravity (determined with helium pycnometer) of the CH sample was measured to be 2.92 g/cm^3, while the corresponding value for the NH sample was measured to be 2.78 g/cm^3.

The XRD composition of NH shows typical peaks that belong to the kaolin group of minerals and high iron oxides content, responsible for the rusty-reddish colour of the material (see Fig. 2 **and** Fig. 3). The XRD study of the CH sample (see Fig. 3-**b**) confirmed alteration of the material after heating, showing decrement of

Table 1

Chemical composition of fly ash, GGBS, and halloysite clay minerals (natural and calcined) determined by XRF.

Material	SiO_2	Al_2O_3	Fe_2O_3	MgO	CaO	Na_2O	K_2O	TiO_2	P_2O_5	SO_3	MnO
Fly ash	53.30	23.70	8.22	1.40	3.77	1.20	2.46	0.95	1.25	1.00	0.06
GGBS	26.90	9.20	0.42	7.83	48.90	0.21	0.21	0.56	1.10	2.79	0.18
Natural halloysite clay minerals	43.80	28.70	18.90	0.10	1.80	0.20	0.12	2.77	1.24	0.13	0.72
Calcined halloysite clay minerals	44.20	29.90	17.50	0.17	2.08	0.34	0.03	2.66	1.06	0.22	0.24
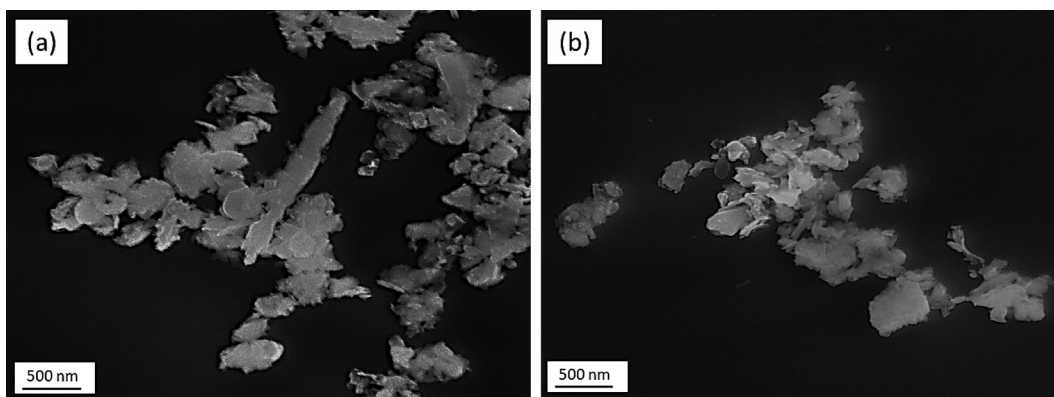
Fig. 1. Microstructure of (a) natural halloysite clay minerals (NH) and (b) calcined halloysite clay minerals (CH).
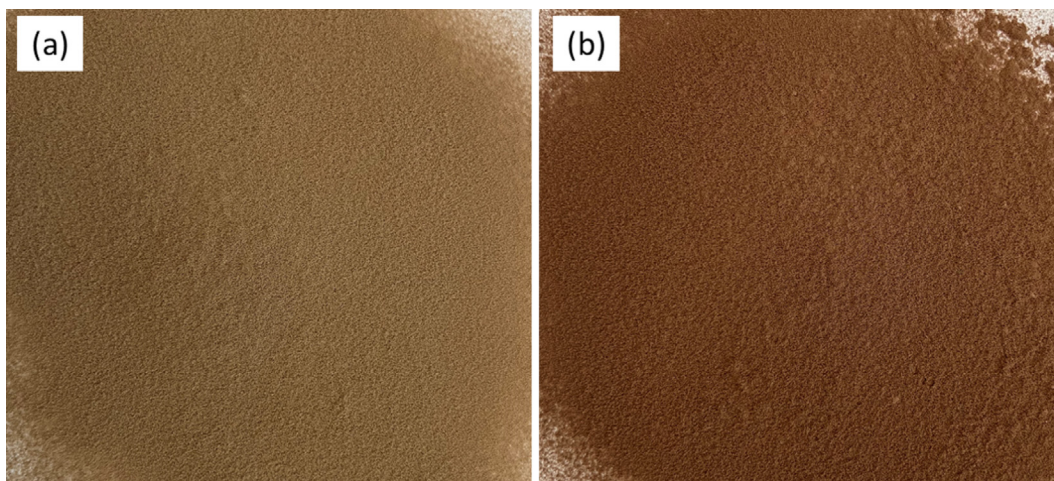
Fig. 2. Visual appearance of (a) natural halloysite clay minerals (NH) and (b) calcined halloysite clay minerals (CH).
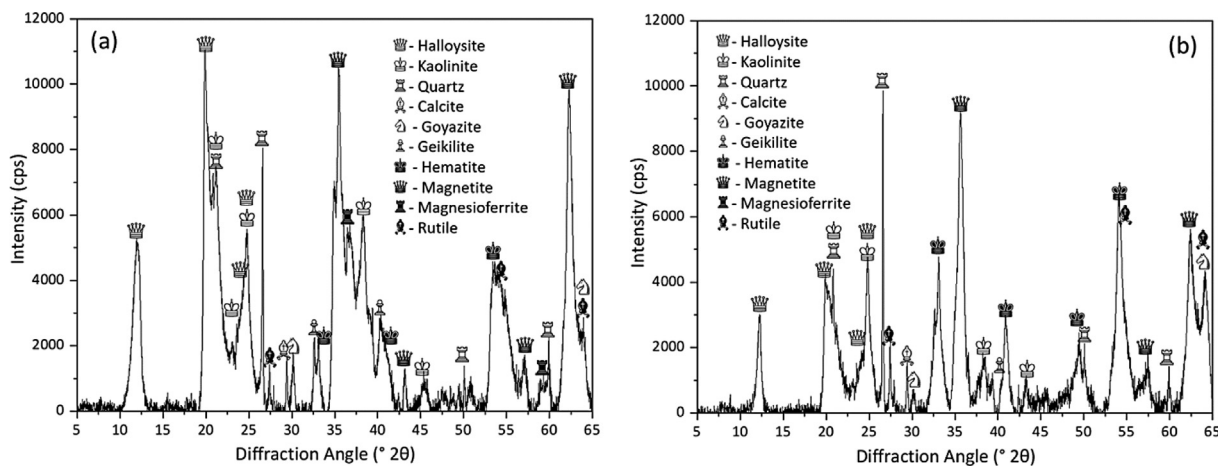
Fig. 3. Post-processed X-ray diffraction patterns of (a) natural halloysite clay minerals (NH) and (b) calcined halloysite clay minerals (CH).
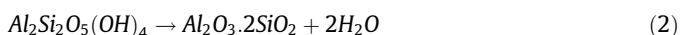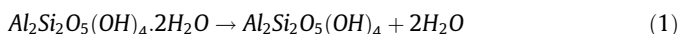
the halloysite peaks, which confirms that the material underwent dehydroxylation [26].

TG analysis shows three mass loss events for the NH sample, labelled as 1, 2 and 3 in Fig. 4, and two mass losses, labelled as 1 and 3, for the CH sample. Detailed information on the detected mass losses is presented in Table 2.

Mass loss No. 1 of the NH sample (1.8 wt%) can be attributed to the evaporation of absorbed water, while mass loss No. 2 (2.4 wt%) is assigned to the dehydration of the material according to **Eq. (1)** [26,27].

Mass loss No. 3 (8.5 wt%) is assigned to the removal of the inter-layer water of HNT-raw according to **Eq. (2)**.

$$Al_2Si_2O_5(OH)_4.2H_2O \rightarrow Al_2Si_2O_5(OH)_4 + 2H_2O \qquad (1)$$

$$Al_2Si_2O_5(OH)_4 \rightarrow Al_2O_3.2SiO_2 + 2H_2O \qquad (2)$$

For the CH sample, only the mass loss events attributed to the evaporation of absorbed water and the removal of interlayer water (mass losses Nos. 1 and 3 in Fig. 4, respectively) were observed. This indicates that during calcination at 600 °C for 1 h, NH was completely dehydrated, while not all the interlayer water was removed. According to the mass loss ratios of NH and CH attributed to the removal of interlayer water, about 60 wt-% of the interlayer water containing halloysite available in the NH sample was dehy-droxylated during calcination.

The results of surface functional groups on the NH and CH samples are presented in FTIR spectra in Fig. 5. The bands at 3621 cm^{-1} and 3694 cm^{-1} reported for NH are typical to all kaolin minerals and are attributed to the inner hydroxyl groups and the inner-surface hydroxyl groups, respectively. The band at 3546 cm^{-1} is attributed to surface-adsorbed water [28]. These bands are absent in dehydrated halloysite (CH). The signal at 1650 cm^{-1} is attributed to the bending vibrations of water molecules [21]. The bands in the range of 1100–400 cm^{-1} are associated with the aluminosilicate structure of the material and are linked with the vibrations of the Si—O—Si(Al) bridges [29], while the one at 917 cm^{-1} is attributed to O-H deformation of inner hydroxyl Al-OH groups [30]. The CH sample exhibited some apparent differences because of dihy-droxylation. This phenomenon is attributed to the progressive dis-ordering of the calcined halloysite at high temperatures [31,32].
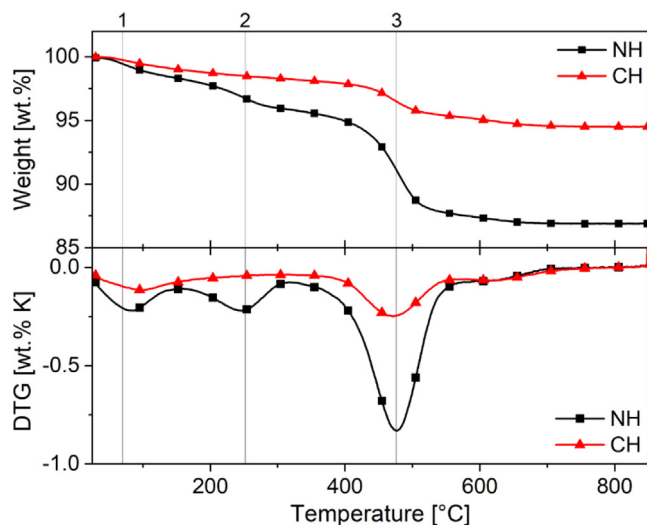

Fig. 4. TG and DTG curves of natural halloysite clay minerals (NH) and calcined halloysite clay minerals (CH).

3. Experimental methods

3.1. *Mixing* procedure **and sample preparations**

Based on the author's previous studies [9,11,33], AAMs were prepared by dry-mixing source materials, aggregates, and clay additives for 5 min at 350 rpm in a planetary mixer (Kenwood, Germany). After dry mixing, the alkaline solution was gradually added to the solid ingredients with a constant alkaline solution/ source material (fly ash + slag) ratio of 0.4 and mixed at 450 rpm for another 10 min. It should be mentioned that a constant aggregate to binder ratio of 1.65 was considered in all mix formulations. Table 3 shows the mixture formulations. Thereupon, AAM mixtures were poured into prismatic moulds measuring $40 \times 40 \times 160$ mm3 for cast samples or into the hopper of a 3D printer for the printing process. Based on the author's previous works and other literatures [9,11,34,35], both cast and printed specimens were immediately heat-cured for 24 h at 60 °C. Following that, the samples were kept at an ambient temperature of 20 ± 3 °C (air-curing) for additional six days. Fig. 6 illustrates the experimental framework in this investigation.

3.2. Printing procedure

A gantry 3D printer with a custom-designed auger extruder and a 20 mm circular-shaped nozzle was employed, similar to the authors' previous studies [9,11]. The printing parameters, including motion speed and nozzle standoff, were adjusted to 15 mm/s and 10 mm, respectively. The printable mix compositions were first printed in $250 \times 200 \times 40$ mm^3 rectangular slabs. Then, three $160 \times 40 \times 40$ mm^3 prisms for each composition were cut and extracted to keep the printed and cast samples consistent.

3.3. Materials characterisations

3.3.1. X-ray diffraction

The XRD experiments were performed using an X-ray diffrac-tometer (Empyrean, PANanlytical) in Bragg-Brentano geometry, equipped with CuKα X-ray tube. A programmable divergence slit in the incident beam path, and a programmable anti-scatter slit in the diffracted beam path were applied (irradiated/observed length 15.0 mm). One scan was performed during a measurement time of 1 h in the 2Θ range from 5° to 65°.

#### 3.3.2. Derivative Thermogravimetry

Derivative Thermogravimetry (TGA/DTG) measurements were performed using a TG209 F3 Tarsus, Netzsch. During the measurements, 10 mg of natural and calcined halloysite samples were heated at the 10 K/min rate up to a maximum temperature of 850 °C. The sample chamber was purged with N$_2$ during the entire measurement time. Weight losses in each step were determined by the tangential method.

3.3.3. *Fourier* transform **infrared spectroscopy**

A Fourier transform infrared spectroscopy-Attenuated total reflectance (FTIR-ATR) using PerkinElmer Spectrum one Spectrometer, UK test was conducted to record the infrared spectra of natural and calcined halloysite materials and the AAMs. The infrared spectra were obtained in the range of 4000–550 cm^{-1} with a resolution of 4 cm^{-1} using an attenuated total reflection instrument with a 3x bounce diamond crystal at a 45° incidence angle. All AAM samples were dried and powdered before the measurements, and the average result of a batch of three samples was reported for each composition.

Table 2
Mass losses of the NH and CH samples measured by TGA.

Sample	Mass loss event	Onset (°C)	Mid (°C)	End (°C)	Mass Loss (wt.%)
NH	1	30	81	160	1.8
	2	160	252	321	2.4
	3	321	476	608	8.5
CH	1	30	89	215	1.4
	3	316	468	575	3.4
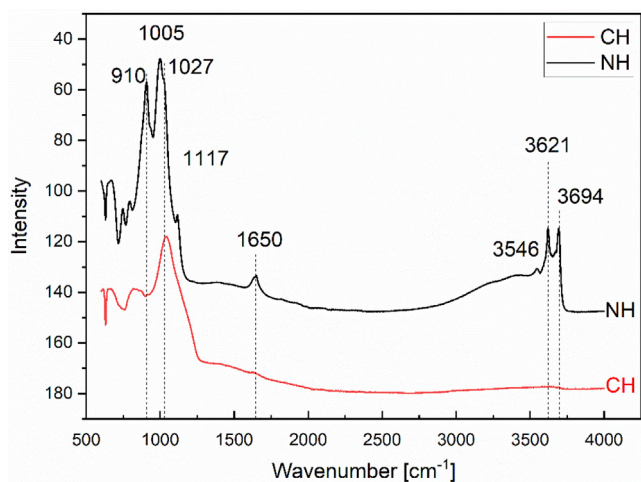
Fig. 5. Fourier transform infrared (FTIR) spectroscopy graph of natural (NH) halloysite clay minerals and calcined (CH) halloysite clay minerals.

3.3.4. Microstructure *analysis*

The microstructure of the AAM samples, was investigated using a Hitachi TM3000 Scanning Electron Microscope (SEM). To analyse the microstructure of AAM samples, for each composition, a minimum of ten samples with the approximate size of 10 mm³ was cut using the broken portions of samples in the flexural strength test. The microscope was operated under an accelerating voltage of 15 kV.

3.4. Extrusion window (open time)

The extrusion window test of AAMs was conducted to determine ideal 3D printing period of each composition. The extrusion window is defined as the period when fresh AAM's workability remained at a level that enabled it to be extruded. The extrusion window was measured by printing a 250 mm long straight-lined filament after the rest time intervals of 5 min until the discontinuity of the printed filament occurred, and the mixture was no longer extrudable.

3.5. *Shape* retention

The unconfined compression test was used in this study to determine the shape retention of fresh AAMs (see Fig. 7). The fresh mixture was filled into a plastic cylinder of 70 mm diameter and 100 mm height and tamped lightly in each test. The plastic cylinder was lifted after two min, and the shape retention of the freestanding mixtures was monitored using an Instron device coupled with a 3 KN loadcell. The fresh cylindrical specimen was loaded at the load rate of 10 mm/min until it reached 30 mm of compaction. The aforementioned values were determined through a series of trial and error to determine the strength of fresh AAMs when the top layer was deposited on top of the first layer. The hopper's extrusion force was approximately stimulated by the 10 mm/min load rate. Instron hydraulic press guarantees the uniform pressure distribution on top of the fresh mixture. The maximum force after 30 mm of compaction was recorded. These force values were utilised to compare the shape stability for various fresh mixtures.

3.6. Mechanical *properties*

The mechanical performance of the cast and the printed samples was evaluated using a 150 kN universal testing machine (Instron 5960, UK) at a constant loading rate of 1 mm/min, following EN 196–1:2016. A three-point bending test on the 160 × 40 × 40 mm prisms with a span distance of 100 mm was used to determine the flexural strengths. The compressive strength was measured on the 40 mm cubes utilising the fractured portions of the specimens in a flexural strength test. The average results obtained from three samples with the loading direction perpendic-

Table 3
Mixture formulations of AAM modified with natural (NH) and calcined (CH) halloysite additives.

| Sample ID	Source materials (wt.%)		Activator to source materials (FA + GGBS) ratio	Aggregate (wt.%)			Additive (wt.%)		Na₂SiO₃ to NaOH ratio
				River sand		Quartz sand			
	FA	GGBS		0–0.5 mm	0.5–1 mm		NH	CH	
Control	67	33	0.4	53	36	11	0	0	2:1
NH-0.5	67	33	0.4	53	36	11	0.5	0	2:1
NH-1	67	33	0.4	53	36	11	1	0	2:1
NH-1.5	67	33	0.4	53	36	11	1.5	0	2:1
NH-2	67	33	0.4	53	36	11	2	0	2:1
NH-3	67	33	0.4	53	36	11	3	0	2:1
NH-5	67	33	0.4	53	36	11	5	0	2:1
CH-0.5	67	33	0.4	53	36	11	0	0.5	2:1
CH-1	67	33	0.4	53	36	11	0	1	2:1
CH-1.5	67	33	0.4	53	36	11	0	1.5	2:1
CH-2	67	33	0.4	53	36	11	0	2	2:1
CH-3	67	33	0.4	53	36	11	0	3	2:1
CH-5	67	33	0.4	53	36	11	0	5	2:1
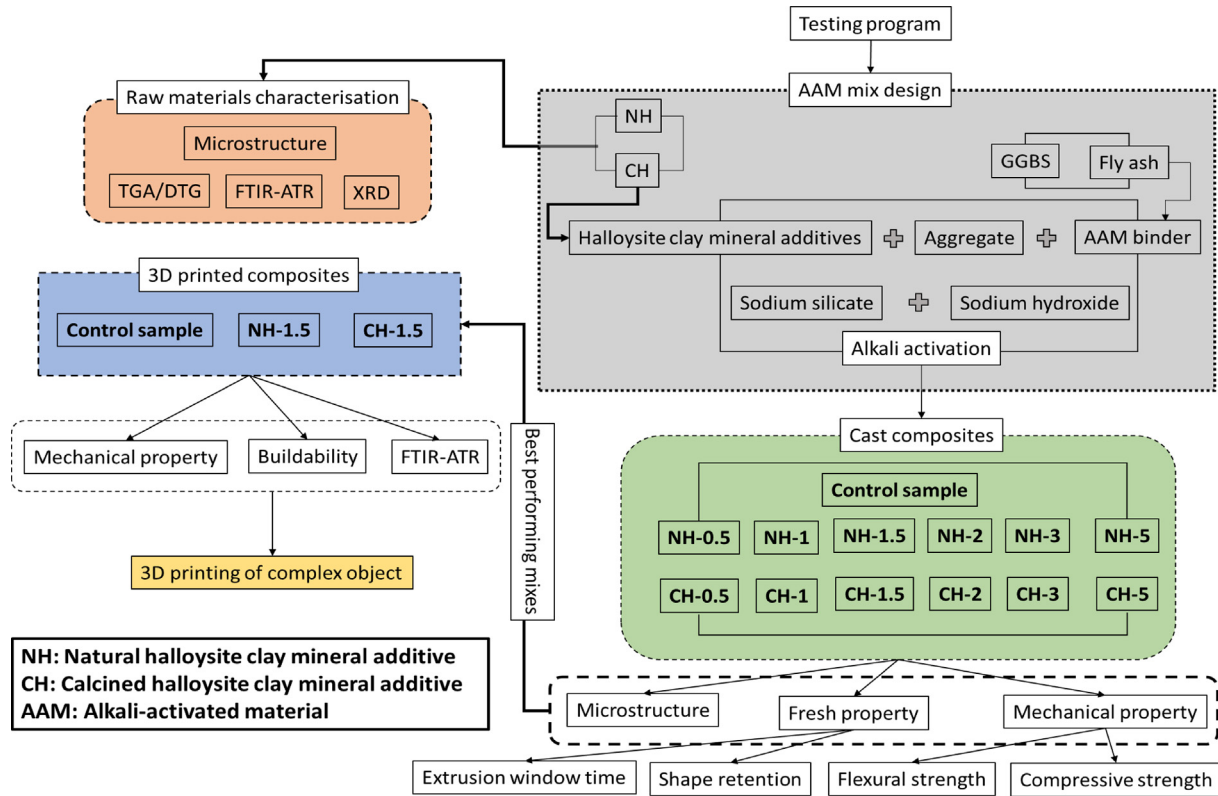
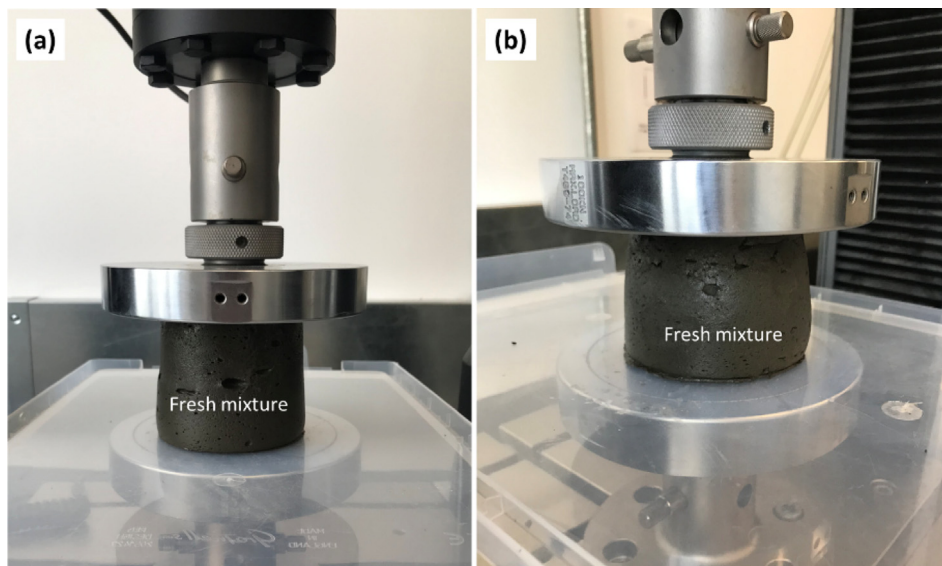**Fig. 6.** Experimental framework and detailed steps for this study.

Fig. 7. Experimental setup for shape retention test of the fresh mixture, (a) before loading and (b) after loading.

ular to the printing path is used to calculate compressive and flexural strengths.

3.7. Buildability **test**

An ad-hoc testing method was employed by printing 15 layers of selected AAMs in a circular-shaped printing path with a diameter of 150 mm. High-quality footage of the printed samples was recorded to visually examine the buildability of selected mixtures in terms of maximum height of printed objects, vertical/radial distortion, and individual layer deformation. The best performing mixture was

then selected to print a twisted-column (see Fig. 15) to demonstrate the feasibility of the developed AAM composite to build complex geometries.

4. Results and discussion

4.1. Mechanical **properties of cast samples**

Fig. 8 shows the flexural and compressive strengths of AAMs with 0 to 5 wt-% NH and CH additives after seven days of curing.
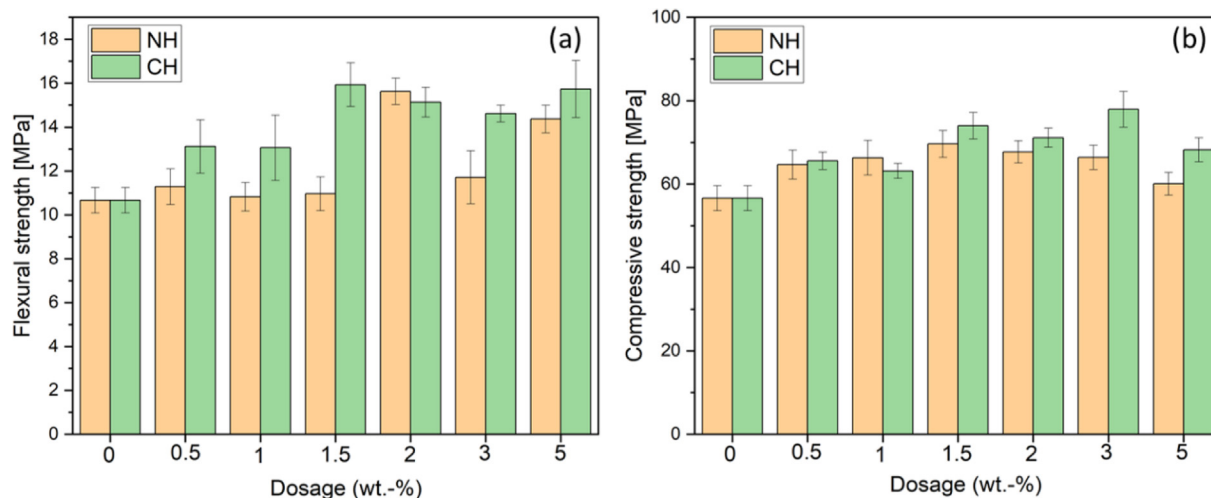
Fig. 8. (a) Flexural and (b) compressive strengths of AAMs modified with natural (NH) and calcined (CH) halloysite. Note the reported results are for cast specimens. The error bars show ± 1.0 Standard Deviation.

As shown in Fig. 8-**a**, the flexural strength of the samples containing NH particles was up to about 46% higher than that of the control mixture. The flexural strength of all CH-modified AAMs exhibited higher values to the control sample. The highest flexural strength was registered for the CH-1.5 and CH-5 mixtures with around 50% improvement in both compositions, compared to the control sample.

As shown in Fig. 8-**b**, the incorporation of 1.5 wt%, 2 wt% and 3 wt% of the CH additive (in the CH-1.5, CH-2 and CH-3 mixtures) displayed 30%, 25%, and 38% enhancements in the compressive strength of AAMs, respectively compared to that of the control sample. The compressive strength results (see Fig. 8-**b**) revealed that the mean compressive strength of the CH-modified AAMs (except the CH-1 mixture) was higher than the NH-modified counterparts. It can be argued that for 0.5 wt%, 1 wt%, 1.5 wt% and 2 wt% of halloysite clay minerals additives the difference in compressive strength between the CH– and NH-modified AAMs was within the scatter of the results. It is evidenced that the effect of CH incorporation is more significant compared to NH in flexural strength rather than compressive strength. According to several studies [36–38], the flaky, elongated, thin, and platy shape of nano-clay particles provides the crack bridging and blocking effect, preventing the propagation of microcracks within cementitious composites and thereby increasing tensile resistivity. As a result, the crack bridging and crack blocking effects are maximised by the better dispersion of CH particles compared to NH particles, resulting in more significant improvements in the flexural strength of the CH-modified AAMs compared to their NH-modified counterparts. Similar effects on flexural strength has been reported for instance by Liu et al. [39].

In a research conducted by Assaedi et al. [40], the samples, modified with 2 wt% Cloisite 30B exhibited improvements of 20% and 23% in geopolymer composite's flexural and compressive strength, respectively, which agree with the level of enhancement obtained in mechanical properties of CH-modified composites in the current study. Several authors [40–42] reported that enhancements in the mechanical properties of nano-clay-modified AAM composites could be attributed to several reasons. Firstly, nano-clay incorporation provides more available silica and alumina sources within mixtures, accelerating the alkali-reaction function. This results in more activation products and fewer unreacted fly ash due to the increased AAM's amorphous content. In addition to the extra amorphous aluminosilicate supply from the nano-

clay particles, the added nano-clay serve as a seeding site for AAM, improving the morphology structure and mechanical characteristics [43]. For instance, with the addition of nano-clay into the fly ash-based geopolymer, Assaedi et al. [40] reported an enhancement in the geopolymerisation reaction. This enhancement was confirmed by X-ray diffraction (XRD) and Fourier-transform infrared spectroscopy (FTIR) assessments, which indicated increased amorphous substances leading to an improved geopolymeric gel. Second, the adequate dispersion of nano-clay particles within the AAM mixture results in a more compact matrix structure due to decreased porosity [43,44]. However, the structural compaction of AAMs in the presence of CH has shown to be higher than that of NH, suggesting the better pore-filling effect of nano clays in the calcined state. According to a study by Hakamy et al. [25], the calcination process led to the destruction and breaking of numerous nano-clay platelets, resulting in the production of nano-clays with lower dimensions. In this study (see Fig. 1), calcined nano-clays (i.e., CH) with smaller sizes demonstrated a better pore-filling effect and consequently enhanced the compaction of composites to a greater extent compared to the samples containing NH particles. The change of the trend in the flexural and compressive strengths' results after 2 wt% has to be associated with the agglomeration of excessive nano-clay particles in the AAMs. When using a high dosage of nano-clay particles in a geopolymer mixture, the presence of more unreacted particles generates excessive self-desiccation and cracking in the matrix, compromising the mechanical performance of hardened samples [45]. Moreover, agglomerated clay particles can act as defects within the AAM structure, reducing mechanical performance [46]. As shown in Fig. 9, the sample modified with 1.5 wt-% NH particles exhibited a similar morphology to the control sample. In both control and NH compositions, several unreacted fly ash particles, as well as micro-cracks, were observed inside the AAM matrix. In contrast, the morphology of composites modified with 1.5 wt-% CH displayed a more compact microstructure but also show unreacted fly ash. This suggests that the lower dispersion of NH particles plays a dominant role over alkali-reaction acceleration leading to the lower mechanical performance of AAMs reinforced with NH as compared to CH particles.

The FTIR-ATR spectra of the control, NH-1.5 and CH-1.5 mixtures are shown in Fig. 10. The absorption peak at 1644 cm^{-1} represents the free water's stretching vibrations of H-OH bonds corresponding to AAMs' absorbed water [47].The asymmetric
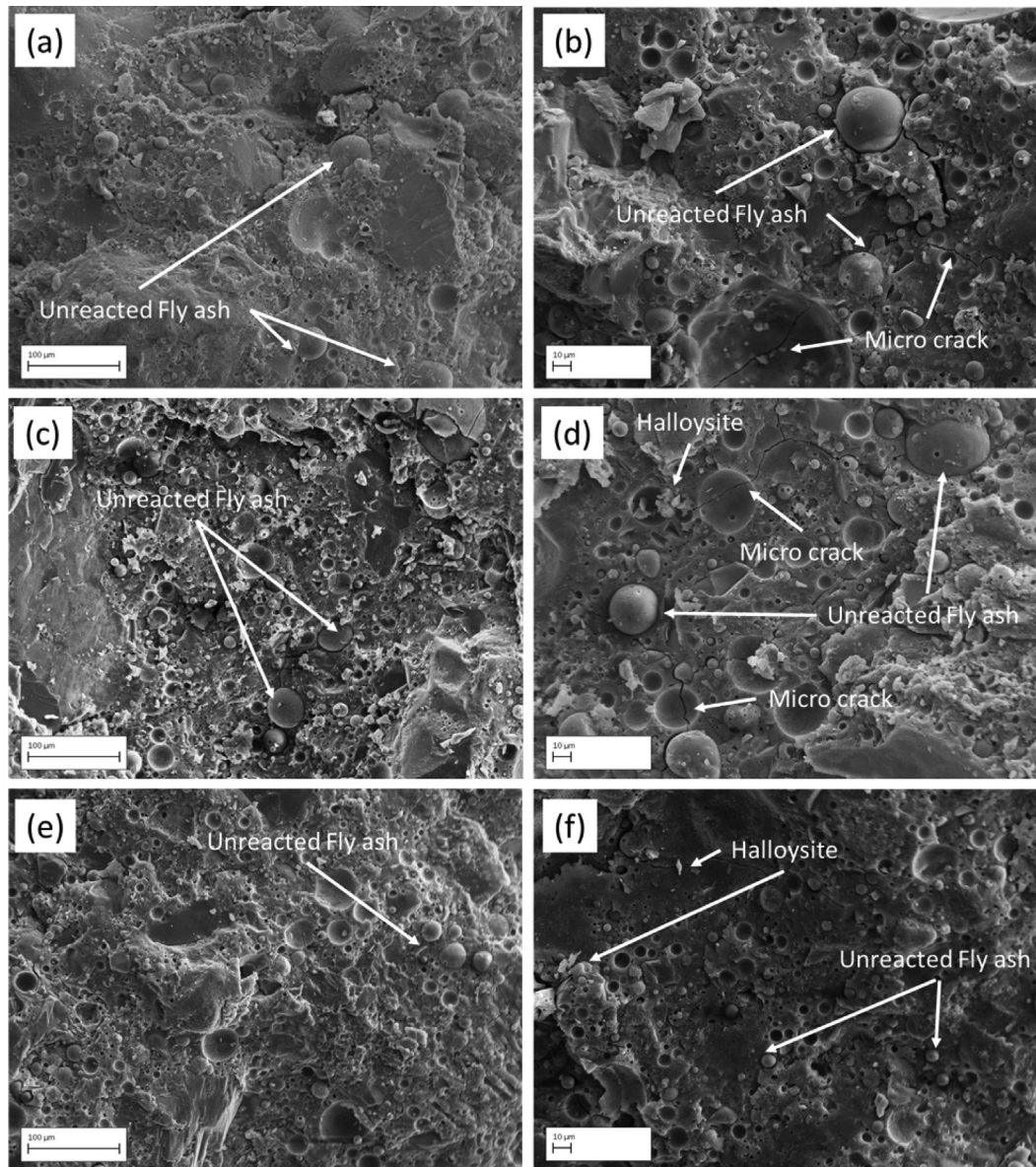
Fig. 9. Microstructure of the cross section of (a) and (b) Control sample, (c) and (d) NH-1.5 sample, and (e) and (f) CH-1.5 sample after flexural strength test. Note the reported results are for cast specimens.

stretching of O-C-O bonds in CO_3^{2-} anion groups (the band around 1430 cm^{-1}) describes the carbonation phenomena during the curing stage of the composite's alkali-activation process [48]. The low intensity of this band suggests little carbonation of the composite. The band at 774 cm^{-1} demonstrates the Al—O amorphous stretching vibration and O—Si—O vibration of AAMs [49]. The quartz Si—O bonds (band at 692 cm^{-1}) indicate the insolubility of quartz particles in the alkali reaction [50]. The peak around 1000 cm^{-1} corresponds to the Si—O—T bonds (T reflects the tetrahedral Al or Si) within the AAM gel [51]. Halloysite clay incorporation results in the silica concentration increase in the composite structure, which is reflected by the slight shift of the peak of the Si—O—T bond from 988 cm^{-1} for the control sample to 1002 cm^{-1} and 1004 cm^{-1} for the NH-1.5 and CH-1.5, respectively [52]. Additionally, it proves an increase in the degree of structural alkali-activation. According to Król et al. [53], detecting the Si—O—T band's peak at lower wavenumbers reveals the increased quantity of aluminium in the tetrahedral positions, thus diminishing the AAM composite's degree of polymerization. This confirms the compressive strength

improvements of NH-1.5 and CH-1.5 composites compared to the control mixture (see Fig. 8-b) [29].

4.2. *Fresh* properties *assessment*

Due to the direct relationship between the extrusion window (open time) parameter and other fresh characteristics of AAMs, this parameter is known as the most applicable and relevant parameter since it effectively simulates the 3D printing process of fresh AAM composites. As shown in Fig. 11 **and** Fig. 12-**a**, increasing the dosage of both natural and calcined clay additives decreased the extrusion window of the AAM mixtures. The extrusion window of the NH-0.5 and NH-1 mixtures was equal to that of the control mixture (45 min). However, the extrusion window decreased to 40 min and 30 min for the NH-1.5 and NH-2 mixtures, respectively. For the CH-modified samples, the extrusion window gradually decreased from 45 min for the CH-0.5 mixture to 40 min, 30 min, and 15 min for CH-1, CH-1.5, and CH-2 mixtures, respectively. As shown in Fig. 12-**a**, the NH– and CH-modified mixtures
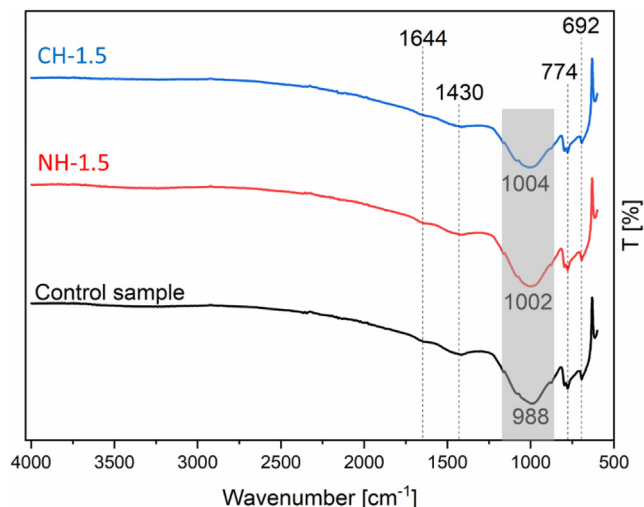
Fig. 10. Fourier transform infrared spectra of the control, NH-1.5, and CH-1.5 composites.
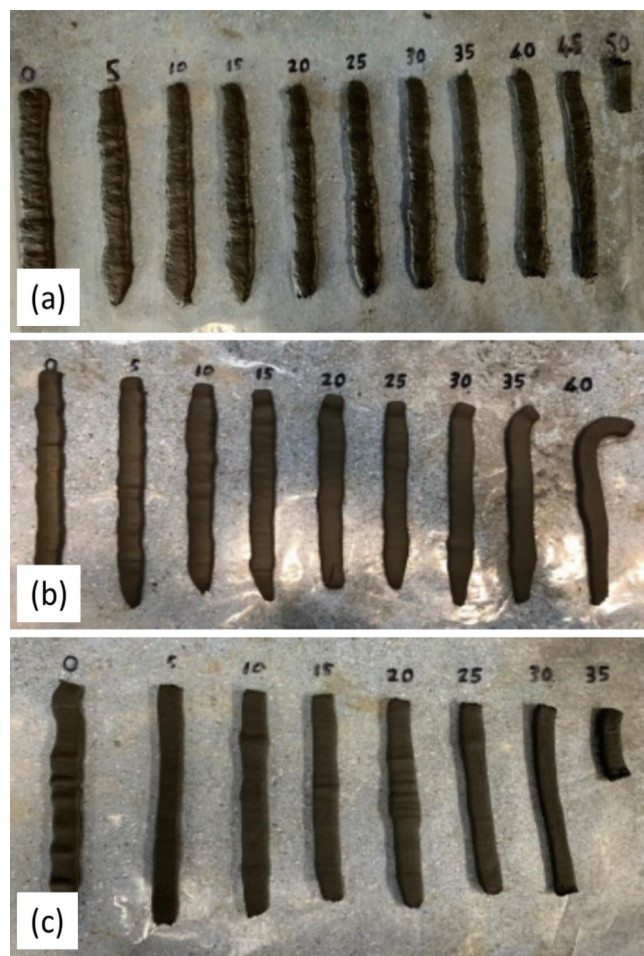

Fig. 11. Extrusion window (open time) of AAM mixtures: (a) Control sample, (b) NH-1.5, and (c) CH-1.5.

containing more than 2 wt% of halloysite clay additives (i.e., the NH-3, NH-5, CH-3 and CH-5 samples) were not extrudable. The incorporation of calcined clay additive exhibited a more substantial influence on diminishing the extrusion window when compared to natural clay additives. According to numerous studies

[15,54,55], cementitious materials' initial setting time and extrusion window (open time) are directly connected. As discussed in **Section 4.2**, the results could be associated with the higher alkali-activation rate of the CH-modified samples compared to the NH-modified counterparts, which results in a faster initial setting of these mixtures. The study of Allalou et al. [56] also focused on the effect of calcined halloysite on initial and final setting time of cementitious composites and they found a descending trend in the initial and final setting times as dosage of calcined halloysite increased.

The results of shape retention test are shown in Fig. 12-**b**. As said above, the NH-3, NH-5, CH-3 and CH-5 samples were not extrudable, and thereby were excluded from the shape retention test. The results suggest that the shape retention capacity of fresh AAM composites was gradually increased by increasing the dosage of both natural and calcined halloysite clay additives compared to the control sample. This is due to the presence of halloysite clay particles with fine particle size and high specific surface area, which leads to the higher free water absorption in the fresh mixture. However, for all mixtures modified with calcined halloysite clay particles, the shape stability is relatively lower than their counterparts reinforced with natural halloysite clay particles. The higher shape retention capacity of the NH-modified composites could be attributed to the existence of hydroxyl (−OH) functional groups in the NH particles (See Fig. 5). This oxygen content functional group absorbs more free water, which leads to increased friction between the solid components of the AAM mixture, creating stiffer mixtures compared to the control sample and the CH-modified composites.

4.3. Mechanical performance of 3D printed samples

Based on aforementioned mechanical properties test results, the mixtures containing 1.5 wt-% calcined halloysite (the CH-1.5 mixture) was selected as viable mixture for 3D printing. Fig. 13 shows the flexural and compressive strengths, of conventionally cast and 3D printed (loading direction is perpendicular to the printing path) of AAM samples containing 1.5 wt-% calcined and natural halloysite clay along with the control sample after 7 days of curing. It should be noted that the control sample and the NH-1.5 were also printed for only the sake of comparison. The superior mechanical performance of the CH-1.5 samples to the NH-1.5 mixture is attributed to the better dispersion of CH particles within the AAM matrix. In NH particles, there is a high tendency of free water absorption, generated by −OH functional groups, which hinders adequate distribution of NH particles in the fresh mixture. This leads to the formation of agglomerated NH particles (see Fig. 8 **and** Fig. 9-**d**) [44,57], which act as a defect and consequently reduce the mechanical properties of the resulting NH-modified AAM composite.

Comparison between cast and printed samples showed that in the control and NH-1.5 mixtures, the flexural strength of the printed samples exhibited a reduction of 14% and 3%, respectively compared to their conventionally cast counterparts. However, the flexural strength reduction of NH-modified samples is negligible. The compressive strength of the printed control sample (i.e., 57.1 MPa) is comparable to that of cast control sample (i.e., 56.6 MPa). In the case of the NH-1.5 mixture, a compressive strength reduction of 14% is registered when compared to its conventionally cast counterpart. On the other hand, incorporating the CH additive increased the flexural and compressive strengths of the printed CH-1.5 samples by 10% and 7%, respectively, compared to the corresponding cast samples. This indicates that the flexural and compressive strengths of 3D printed CH-1.5 samples were 88% and 40%, respectively, higher than those of the printed control samples. The higher mechanical performance of printed CH-1.5
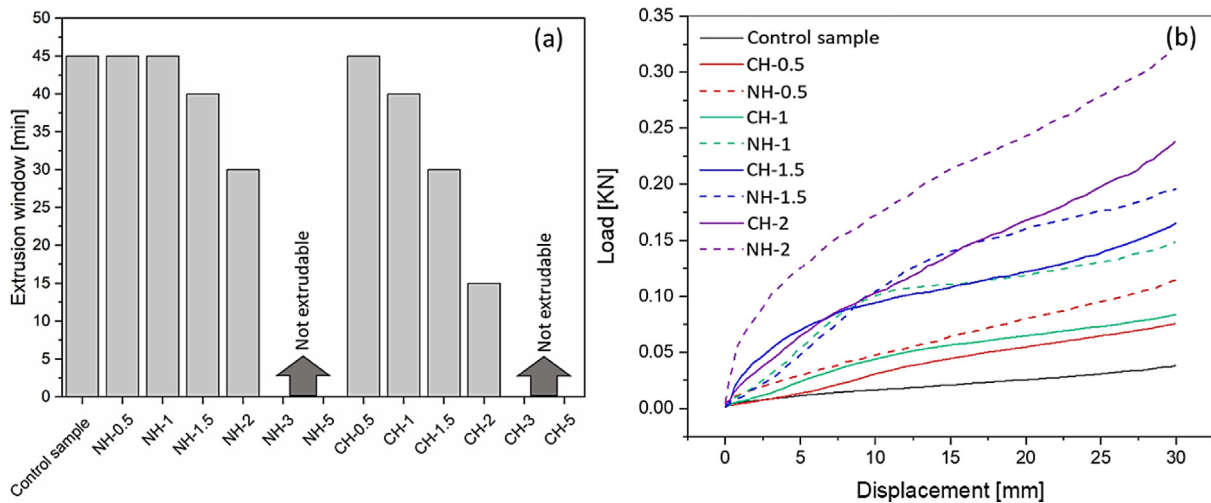
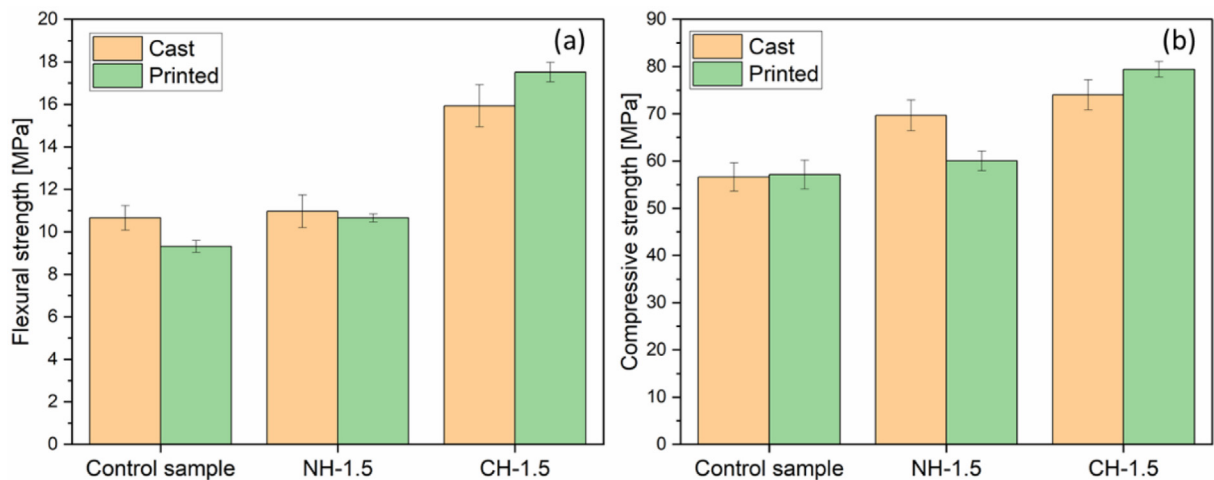**Fig. 12.** Fresh properties of AAM mixtures (a) extrusion window (open time) and (b) shape retention.

Fig. 13. Mechanical properties of cast versus printed samples: (a) flexural strength and (b) compressive strength. Note: The error bars show ± 1.0 Standard Deviation.

compared to its cast counterpart has to be associated with several reasons. According to Nerella et al. [58], two types of compaction, i.e., extrusion and deposited layer's weight compaction, are applied to printed structures. The CH-1.5′s low shape stability, compared to NH-1.5 mixture, generates better compaction in both compaction systems throughout the printing process compared to the traditional cast sample. High compaction during the printing process results in production samples with lower porosity (i.e., denser structure), which enhances mechanical performance. It has been also demonstrated that introducing nano-clay generates thixotropic behaviour, which indicates that the inter-particle bonds within the mixture break under the extrusion shear forces. After printing, the inter-particle bonds are reconstructed more firmly, increasing the AAMs' mechanical performance [12,59]. The high compaction of CH-1.5 during the extrusion process facilitates and intensifies the inter-particle bond reconstruction, improving the mechanical performance.

4.4. Buildability

Fig. 14 shows the buildability performance of the control, CH-1.5 and NH-1.5 mixtures. As shown in Fig. 14-a, a considerable radial distortion and bottom layers height reduction was observed for the control sample. This effect is associated with the compres-

sive load induced by the weight of deposited top layers. However, the higher shape retention of the mixtures modified with clay (both CH-1.5 and NH-1.5) resulted in printed objects with no radial distortion and minimal bottom layers height reduction (see Fig. 14-b and 14-c). A smooth surface finish with no visible segregations was observed on the outer surface of all printed objects.

After deposition of 15 layers, the height of each printed object was measured. The heights of the control, NH-1.5 and CH-1.5 printed objects were measured to be 122 mm, 146 mm, and 143 mm, respectively, while the height of the model was 150 mm. Therefore, it can be concluded that incorporation of both NH and CH halloysite additives significantly enhanced the buildability and shape stability performance of the printed AAMs. Both NH-1.5 and CH-1.5 samples showed almost comparable buildability performance. However, the results of shape retention assessment (see **Section 4.3**) showed that the NH-1.5 mixture had a slightly better shape stability compared to the CH-1.5 mixture (see Fig. 12-**b**, in which the maximum compressive load at 30 mm vertical displacement increased from 40 N for the Control sample to 190 N and 170 N for the NH-1.5 and CH-1.5 samples, respectively).

As reported in several studies [10,60], compared to conventional casting procedure, the capability to fabricate complex 3D objects without the use of formwork is one of the most appealing

Fig. 14. Buildability performance: (a) Control sample, (b) NH-1.5 sample, and (c) CH-1.5 sample.
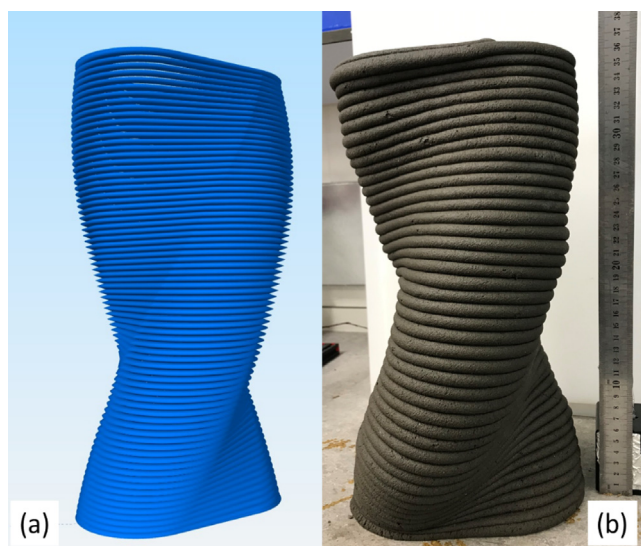

Fig. 15. 3D printing of a twisted column made by the CH-1.5 mixture (a) CAD model and (b) printed object.

characteristics of 3D printing process. The large gap between design and production obliged the architect's community to pursue buildable and financially feasible designs to avoid one-time use of custom moulds and formwork, considerable quantities of waste materials, and unpredicted construction delays. The 3D printing process enables ease of production of complex designs. Fig. 15 depicts a twisted column printed using the CH-1.5 composite containing 1.5 wt% calcined clay, which demonstrated superior hardened properties among other AAM compositions investigated in this study. The twisted column was printed at a motion speed, layer height, and layer width of 15 mm/s, 8 mm, and 30 mm, respectively. The whole printing process took about 22 min. As shown in Fig. 15-**b**, the printed twisted column composed of 45 layers showed no considerable structural distortion and bottom layer deformation.

5. Conclusions

This study reported the effects of natural halloysite (NH) and calcined halloysite (CH) clay additives on the fresh (i.e., open time, shape stability and buildability) and hardened properties (i.e., microstructure, flexural and compressive strengths) of AAMs to identify a suitable composition for 3D printing process. The NH and CH additive materials were comprehensively characterised using XRF, XRD, FTIR, TGA/DTG and SEM. From this research study the following conclusions can be drawn:

- The addition of 1.5 wt% of CH particles induced remarkable enhancements on the flexural and compressive strengths of the printed CH-1.5 samples (i.e., 88% and 40%, respectively) compared to the printed control sample.
- The CH-1.5 mixture also exhibited significantly enhanced buildability and printing quality compared to the printed control mixture. This made the CH-1.5 mixture suitable to print complex members.
- The results indicated substantial differences in the mixtures' fresh and hardened properties comprising the NH additive as compared to the counterpart mixtures containing the CH additive, which occurred due to the calcination process.

This study proved the use of halloysite clay additives as both reinforcing and rheology modifying additives in 3D printed AAMs. The presented results lay the foundation for broader research in the framework of 3D printable AAMs modified with calcined halloysite clay additives. Future work can explore further optimisations on the printable feedstock and performance assessment of complex printed structures.

Data statement.

The data that support the findings of this study are available from the first author Mehdi Chougan and the corresponding author Seyed Hamidreza Ghaffar, upon reasonable request.

Declaration of Competing Interest

The authors declare that they have no known competing financial interests or personal relationships that could have appeared to influence the work reported in this paper.

Acknowledgements

References

[1] P.A.K. Nair, W.L. Vasconcelos, K. Paine, J. Calabria-Holley, A review on applications of sol-gel science in cement, Constr. Build. Mater. 291 (2021), https://doi.org/10.1016/j.conbuildmat.2021.123065 123065.

[2] M. Valente, M. Sambucci, M. Chougan, S.H. Ghaffar, Reducing the emission of climate-altering substances in cementitious materials: a comparison between alkali-activated materials and Portland cement-based composites incorporating recycled tire rubber, J. Clean. Prod. 333 (2022), https://doi.org/10.1016/j.jclepro.2021.130013 130013.

[3] S. Ma, H. Yang, S. Zhao, P. He, Z. Zhang, X. Duan, Z. Yang, D. Jia, Y. Zhou, 3D-printing of architectured short carbon fiber-geopolymer composite, Compos. Part B Eng. 226 (2021), https://doi.org/10.1016/j.compositesb.2021.109348 109348.

[4] Q. Song, J. Su, J. Nie, H. Li, Y. Hu, Y. Chen, R. Li, Y. Deng, The occurrence of MgO and its influence on properties of clinker and cement: a review, Constr. Build. Mater. 293 (2021), https://doi.org/10.1016/j.conbuildmat.2021.123494 123494.

[5] X. Deng, H. Guo, H. Tan, K. Nie, X. He, J. Yang, Y. Wang, J. Zhang, Effect of organic alkali on hydration of GGBS-FA blended cementitious material activated by sodium carbonate, Ceram. Int. 48 (2022) 1611–1621, https://doi.org/10.1016/j.ceramint.2021.09.240.

[6] B. Nematollahi, J. Sanjayan, F.U.A. Shaikh, Synthesis of heat and ambient cured one-part geopolymer mixes with different grades of sodium silicate, Ceram. Int. 41 (2015) 5696–5704, https://doi.org/10.1016/j.ceramint.2014.12.154.

[7] B. Nematollahi, M. Xia, J. Sanjayan, P. Vijay, Effect of type of fiber on inter-layer bond and flexural strengths of extrusion-based 3D printed geopolymer, Mater. Sci. Forum. 939 (2018) 155–162, https://doi.org/10.4028/www.scientific.net/MSF.939.155.

[8] B. Nematollahi, P. Vijay, J. Sanjayan, A. Nazari, M. Xia, V. Naidu Nerella, V. Mechtcherine, Effect of polypropylene fibre addition on properties of geopolymers made by 3D printing for digital construction, Mater. (Basel). 11 (12) (2018) 2352.

[9] M. Chougan, S.H. Ghaffar, P. Sikora, S.Y. Chung, T. Rucinska, D. Stephan, A. Albar, M.R. Swash, Investigation of additive incorporation on rheological, microstructural and mechanical properties of 3D printable alkali-activated materials, Mater. Des. 202 (2021), https://doi.org/10.1016/j.matdes.2021.109574 109574.

[10] B. Panda, S. Ruan, C. Unluer, M.J. Tan, Investigation of the properties of alkali-activated slag mixes involving the use of nanoclay and nucleation seeds for 3D printing, Compos. Part B Eng. 186 (2020) 107826.

[11] M, Chougan, S, Hamidreza Ghaffar, M, Jahanzat, A, Albar, N, Mujaddedi, R, Swash, The influence of nano-additives in strengthening mechanical performance of 3D printed multi-binder geopolymer composites, Constr. Build. Mater. 250 (2020) 118928. https://doi.org/10.1016/j.conbuildmat.2020.118928.

[12] N. Roussel, G. Ovarlez, S. Garrault, C. Brumaud, The origins of thixotropy of fresh cement pastes, Cem. Concr. Res. 42 (2012) 148–157, https://doi.org/10.1016/j.cemconres.2011.09.004.

[13] N. Roussel, Rheological requirements for printable concretes, Cem. Concr. Res. 112 (2018) 76–85, https://doi.org/10.1016/j.cemconres.2018.04.005.

[14] P. Sikora, M. Chougan, K. Cuevas, M. Liebscher, V. Mechtcherine, S.H. Ghaffar, M. Liard, D. Lootens, P. Krivenko, M. Sanytsky, D. Stephan, The effects of nano- and micro-sized additives on 3D printable cementitious and alkali-activated composites: a review, Appl. Nanosci. 12 (4) (2022) 805–823.

[15] B. Panda, C. Unluer, M. Jen, Extrusion and rheology characterization of geopolymer nanocomposites used in 3D printing, Compos. Part B. 176 (2019), https://doi.org/10.1016/j.compositesb.2019.107290 107290.

[16] S. Allalou, R. Kheribet, A. Benmounah, Effects of calcined halloysite nano-clay on the mechanical properties and microstructure of low-clinker cement mortar, Case Stud. Constr. Mater. 10 (2019), https://doi.org/10.1016/j.cscm.2018.e00213 e00213.

[17] M.S. Kamal, S.A. Razzak, M.M. Hossain, Catalytic oxidation of volatile organic compounds (VOCs) - a review, Atmos. Environ. 140 (2016) 117–134, https://doi.org/10.1016/j.atmosenv.2016.05.031.

[18] M.J. Saif, H.M. Asif, M. Naveed, Properties and modification methods of halloysite nanotubes: a state-of-The-art review, J. Chil. Chem. Soc. 63 (2018) 4109–4125, https://doi.org/10.4067/s0717-97072018000304109.

[19] S. Filice, C. Bongiorno, S. Libertino, G. Compagnini, L. Gradon, D. Iannazzo, A. La Magna, S. Scalese, Structural characterization and adsorption properties of dunino raw halloysite mineral for dye removal from water, Mater. (Basel). 14 (2021) 1–21, https://doi.org/10.3390/ma14133676.

[20] E. Joussein, S. Petit, J. Churchman, B. Theng, D. Righi, B. Delvaux, Halloysite clay minerals — a review, Clay Miner. 40 (2005) 383–426, https://doi.org/10.1180/0009855054040180.

[21] J. Kurczewska, M. Cegłowski, G. Schroeder, PAMAM-halloysite Dunino hybrid as an effective adsorbent of ibuprofen and naproxen from aqueous solutions, Appl. Clay Sci. 190 (2020), https://doi.org/10.1016/j.clay.2020.105603 105603.

[22] E, Joussein, Geology and Mineralogy of Nanosized Tubular Halloysite, 1st ed., Elsevier Ltd., 2016. https://doi.org/10.1016/B978-0-08-100293-3.00002-9.

[23] P. Franciszczak, I. Taraghi, S. Paszkiewicz, A. Meljon, E. Piesowicz, M. Burzyński, Effect of halloysite nanotube on mechanical properties, thermal stability and morphology of polypropylene and polypropylene/short kenaf fibers hybrid biocomposites, Mater. (Basel). 13 (2020) 1–13, https://doi.org/10.3390/ma13194459.

[24] M. Mrówka, M. Szymiczek, T. Machoczek, J. Lenża, J. Matusik, P. Sakiewicz, M. Skonieczna, The influence of halloysite on the physicochemical, mechanical and biological properties of polyurethane-based nanocomposites, Polimery/Polymers. 65 (2020) 784–791, https://doi.org/10.14314/polimery.2020.11.5.

[25] A. Hakamy, F.U.A. Shaikh, I.M. Low, Characteristics of nanoclay and calcined nanoclay-cement nanocomposites, Compos. Part B Eng. 78 (2015) 174–184, https://doi.org/10.1016/j.compositesb.2015.03.074.

[26] L, Andrini, R, Moreira Toja, M.S, Conconi, F.G, Requejo, N.M, Rendtorff, Halloysite nanotube and its firing products: Structural characterization of halloysite, metahalloysite, spinel type silicoaluminate and mullite, J. Electron Spectros. Relat. Phenomena. 234 (2019) 19–26. https://doi.org/10.1016/j.elspec.2019.05.007.

[27] H. Cheng, Q. Liu, J. Yang, J. Zhang, R.L. Frost, Thermal analysis and infrared emission spectroscopic study of halloysite-potassium acetate intercalation compound, Thermochim. Acta. 511 (2010) 124–128, https://doi.org/10.1016/j.tca.2010.08.003.

[28] J.T, Kloprogge, Characterisation of Halloysite by Spectroscopy, 1st ed., Elsevier Ltd., 2016. https://doi.org/10.1016/B978-0-08-100293-3.00006-6.

[29] O. Biel, P. Rożek, P. Florek, W. Mozgawa, M. Król, Alkaline activation of kaolin group minerals, Crystals. 10 (4) (2020) 268.

[30] B. Szczepanik, P. Słomkiewicz, M. Garnuszek, K. Czech, D. Banaś, A. Kubala-Kukuś, I. Stabrawa, The effect of chemical modification on the physico-chemical characteristics of halloysite: FTIR, XRF, and XRD studies, J. Mol. Struct. 1084 (2015) 16–22.

[31] P, Yuan, Thermal-Treatment-Induced Deformations and Modifications of Halloysite, 1st ed., Elsevier Ltd., 2016. https://doi.org/10.1016/B978-0-08-100293-3.00007-8.

[32] C.R. Kaze, T. Alomayri, A. Hasan, S. Tome, G.L. Lecomte-Nana, J.G.D. Nemaleu, H.K. Tchakoute, E. Kamseu, U.C. Melo, H. Rahier, Reaction kinetics and rheological behaviour of meta-halloysite based geopolymer cured at room temperature: effect of thermal activation on physicochemical and microstructural properties, Appl. Clay Sci. 196 (2020), https://doi.org/10.1016/j.clay.2020.105773 105773.

[33] A. Albar, M. Chougan, M.J. Al- Kheetan, M.R. Swash, S.H. Ghaffar, Effective extrusion-based 3D printing system design for cementitious-based materials, Results Eng. 6 (2020), https://doi.org/10.1016/j.rineng.2020.100135 100135.

[34] B.H. Mo, H. Zhu, X.M. Cui, Y. He, S.Y. Gong, Effect of curing temperature on geopolymerization of metakaolin-based geopolymers, Appl. Clay Sci. 99 (2014) 144–148, https://doi.org/10.1016/j.clay.2014.06.024.

[35] M. Chougan, S.H. Ghaffar, P. Sikora, E. Mijowska, W. Kukułka, D. Stephan, Boosting Portland cement-free composite performance via alkali-activation and reinforcement with pre-treated functionalised wheat straw, Ind. Crops Prod. 178 (2022) 114648.

[36] P. Hosseini, A. Afshar, B. Vafaei, A. Booshehrian, E. Molaei Raisi, A. Esrafili, Effects of nano-clay particles on the short-term properties of self-compacting concrete, Eur. J. Environ. Civ. Eng. 21 (2017) 127–147, https://doi.org/10.1080/19648189.2015.1096308.

[37] N, Hamed, M.S, El-Feky, M, Kohail, E.S.A.R, Nasr, Effect of nano-clay de-agglomeration on mechanical properties of concrete, Constr. Build. Mater. 205 (2019) 245–256, https://doi.org/10.1016/j.conbuildmat.2019.02.018.

[38] A.E. Al-Salami, M.S. Morsy, S. Taha, H. Shoukry, Physico-mechanical characteristics of blended white cement pastes containing thermally activated ultrafine nano clays, Constr. Build. Mater. 47 (2013) 138–145, https://doi.org/10.1016/j.conbuildmat.2013.05.011.

[39] H. Liu, J. Jin, Y. Yu, H. Liu, S. Liu, J. Shen, X. Xia, H. Ji, Influence of halloysite nanotube on hydration products and mechanical properties of oil well cement slurries with nano-silica, Constr. Build. Mater. 247 (2020), https://doi.org/10.1016/j.conbuildmat.2020.118545 118545.

[40] H. Assaedi, F.U.A. Shaikh, I.M. Low, Effect of nano-clay on mechanical and thermal properties of geopolymer, J. Asian Ceram. Soc. 4 (2016) 19–28, https://doi.org/10.1016/j.jascer.2015.10.004.

[41] H. Khater, Effect of Nano-Clay on Alkali Activated Water-Cooled Slag Geopolymer, Br. J. Appl. Sci. Technol. 3 (2013) 764–776, https://doi.org/10.9734/bjast/2014/2690.

[42] N.B. Singh, S.K. Saxena, M. Kumar, Effect of nanomaterials on the properties of geopolymer mortars and concrete, Mater. Today Proc. 5 (2018) 9035–9040, https://doi.org/10.1016/j.matpr.2017.10.018.

[43] M.M. Hassaan, H.M. Khater, M.S. El-Mahllawy, A.M. El Nagar, Production of geopolymer composites enhanced by nano-kaolin material, J. Adv. Ceram. 4 (2015) 245–252, https://doi.org/10.1007/s40145-015-0156-y.

[44] B.B. Jindal, R. Sharma, The effect of nanomaterials on properties of geopolymers derived from industrial by-products: a state-of-the-art review, Constr. Build. Mater. 252 (2020), https://doi.org/10.1016/j.conbuildmat.2020.119028 119028.

[45] A. Ravitheja, N.L.N. Kiran Kumar, A study on the effect of nano clay and GGBS on the strength properties of fly ash based geopolymers, Mater. Today Proc. 19 (2019) 273–276, https://doi.org/10.1016/j.matpr.2019.06.761.

[46] A. Bauluz, F.U.A. Shaikh, I.M. Low, Thermal and mechanical properties of NaOH treated hemp fabric and calcined nanoclay-reinforced cement nanocomposites, Mater. Des. 80 (2015) 70–81, https://doi.org/10.1016/j.matdes.2015.05.003.

[47] S.A. Bernal, J.L. Provis, V. Rose, R. Mejía De Gutierrez, Evolution of binder structure in sodium silicate-activated slag-metakaolin blends, Cem. Concr. Compos. 33 (2011) 46–54, https://doi.org/10.1016/j.cemconcomp.2010.09.004.

[48] M.F. Zawrah, H.A. Badr, R.M. Khattab, H.E.H. Sadek, S.E. Abo Sawan, A.A. El-Kheshen, Fabrication and characterization of non-foamed and foamed geopolymers from industrial waste clays, Ceram. Int. 47 (2021) 29320–29327, https://doi.org/10.1016/j.ceramint.2021.07.097.

[49] A. Fernández-Jiménez, A. Palomo, Composition and microstructure of alkali activated fly ash binder: effect of the activator, Cem. Concr. Res. 35 (2005) 1984–1992, https://doi.org/10.1016/j.cemconres.2005.03.003.

[50] Q. Wan, F. Rao, S. Song, D.F. Cholico-González, N.L. Ortiz, Combination formation in the reinforcement of metakaolin geopolymers with quartz sand, Cem. Concr. Compos. 80 (2017) 115–122, https://doi.org/10.1016/j.cemconcomp.2017.03.005.

[51] A. Palomo, M.T. Blanco-Varela, M.L. Granizo, F. Puertas, T. Vazquez, M.W. Grutzeck, Chemical stability of cementitious materials based on metakaolin - Isothermal conduction calorimetry study, Cem. Concr. Res. 29 (1999) 997–1004, https://doi.org/10.1016/S0008-8846(99)00074-5.

[52] L. Zheng, W. Wang, Y. Shi, The effects of alkaline dosage and Si/Al ratio on the immobilization of heavy metals in municipal solid waste incineration fly ash-based geopolymer, Chemosphere. 79 (2010) 665–671, https://doi.org/10.1016/j.chemosphere.2010.02.018.

[53] M. Król, P. Rożek, D. Chlebda, W. Mozgawa, ATR/FT-IR studies of zeolite formation during alkali-activation of metakaolin, Solid State Sci. 94 (2019) 114–119, https://doi.org/10.1016/j.solidstatesciences.2019.06.004.

[54] T.T. Le, S.A. Austin, S. Lim, R.A. Buswell, A.G.F. Gibb, T. Thorpe, Mix design and fresh properties for high-performance printing concrete, Mater. Struct. Constr. 45 (2012) 1221–1232, https://doi.org/10.1617/s11527-012-9828-z.

[55] R. Lediga, D. Kruger, Optimizing concrete mix design for application in 3D printing technology for the construction industry, Solid State Phenom. 263 (2017) 24–29, https://doi.org/10.4028/www.scientific.net/SSP.263.24.

[56] S. Allalou, R. Kheribet, A. Benmounah, Case studies in construction materials effects of calcined halloysite nano-clay on the mechanical properties and microstructure of low-clinker cement mortar, Case Stud. Constr. Mater. 10 (2019), https://doi.org/10.1016/j.cscm.2018.e00213 e00213.

[57] H. Assaedi, F.U.A. Shaikh, I.M. Low, Characterizations of flax fabric reinforced nanoclay-geopolymer composites, Compos. Part B Eng. 95 (2016) 412–422, https://doi.org/10.1016/j.compositesb.2016.04.007.

[58] V.N. Nerella, S. Hempel, V. Mechtcherine, Effects of layer-interface properties on mechanical performance of concrete elements produced by extrusion-based 3D-printing, Constr. Build. Mater. 205 (2019) 586–601, https://doi.org/10.1016/j.conbuildmat.2019.01.235.

[59] B. Panda, S. Ruan, C. Unluer, M. Jen, Improving the 3D printability of high volume fl y ash mixtures via the use of nano attapulgite clay, Compos. Part B 165 (2019) 75–83, https://doi.org/10.1016/j.compositesb.2018.11.109.

[60] C. Gosselin, R. Duballet, P. Roux, N. Gaudillière, J. Dirrenberger, P. Morel, Large-scale 3D printing of ultra-high performance concrete – a new processing route for architects and builders, JMADE. 100 (2016) 102–109, https://doi.org/10.1016/j.matdes.2016.03.097.